Article

Microstructure and crystal order during freezing of supercooled water drops

Check for updates

Armin Kalita[1], Maximillian Mrozek-McCourt[1,5], Thomas F. Kaldawi[1,6], Philip R. Willmott[2,3], N. Duane Loh[4,7,8], Sebastian Marte[1], Raymond G. Sierra[4,9], Hartawan Laksmono[4,10], Jason E. Koglin[2,11], Matt J. Hayes[2], Robert H. Paul[2], Serge A. H. Guillet[2], Andrew L. Aquila[2], Mengning Liang[2], Sébastien Boutet[2] & Claudiu A. Stan[1,4✉]

Supercooled water droplets are widely used to study supercooled water[1,2], ice nucleation[3–5] and droplet freezing[6–11]. Their freezing in the atmosphere affects the dynamics and climate feedback of clouds[12,13] and can accelerate cloud freezing through secondary ice production[14–17]. Droplet freezing occurs at several timescales and length scales[14,18] and is sufficiently stochastic to make it unlikely that two frozen drops are identical. Here we use optical microscopy and X-ray laser diffraction to investigate the freezing of tens of thousands of water microdrops in vacuum after homogeneous ice nucleation around 234–235 K. On the basis of drop images, we developed a seven-stage model of freezing and used it to time the diffraction data. Diffraction from ice crystals showed that long-range crystalline order formed in less than 1 ms after freezing, whereas diffraction from the remaining liquid became similar to that from quasi-liquid layers on premelted ice[19,20]. The ice had a strained hexagonal crystal structure just after freezing, which is an early metastable state that probably precedes the formation of ice with stacking defects[8,9,18]. The techniques reported here could help determine the dynamics of freezing in other conditions, such as drop freezing in clouds, or help understand rapid solidification in other materials.

We investigated the freezing of individual 40-µm-diameter supercooled water drops using the set-up illustrated in Fig. 1. The droplets were injected into a vacuum chamber, in which they cooled rapidly through evaporation, nucleated ice homogeneously and froze. Femtosecond X-ray pulses and nanosecond light pulses arrived simultaneously at the freezing droplets, producing X-ray diffraction patterns and images of single droplets at several times of flight from 6.4 to 7.8 ms after injection. Each droplet was examined only once.

The freezing of the droplets started with ice nucleation around 234–235 K, followed by dendritic crystal growth leading to partial solidification and heating to the melting temperature, then by inward freezing of the remaining liquid, during which the drops grew spicules and sometimes shattered (Extended Data Fig. 1a). These stages of freezing were also observed in studies with varied droplet environments, sizes and cooling rates[14]; see, for example, the supplementary videos in refs. 4,6. The commonality of freezing stages is largely because of the dynamics of dendritic freezing in supercooled water. Dendritic freezing is an extreme thermal process that generates large heat fluxes and thermal gradients on the order of 10 K µm^{-1} at the freezing front[10]. It depends primarily on temperature and is relatively insensitive to the drop's environment[10] for drops larger than 0.1–1 µm, for which the dynamics of dendritic freezing remains approximately the same over a wide range of cooling rates. Dendritic freezing also produces a common

initial state for the later stages of freezing: an ice–liquid mixture at the melting temperature. This mixture fully solidifies by inward freezing if the drop remains in the environment that supercooled it. The duration of inward freezing depends on the environment. For this experiment, we estimated that it is about 1 ms using a finite-element solidification model (Methods and Supplementary Information).
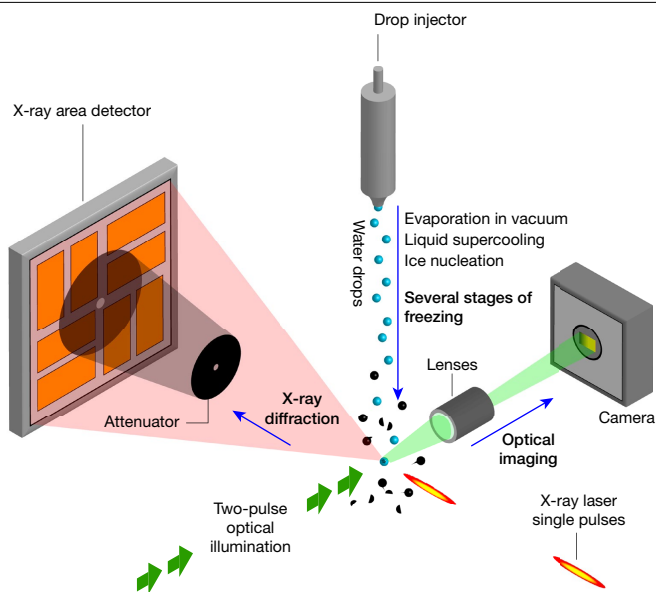
Because both the duration of freezing and the spread of nucleation times were approximately 1 ms, the drops investigated at one time of flight had a broad distribution of freezing stages and we investigated on the order of 1,000 drops at each time of flight to determine the stage probabilities and their temporal evolution. To capture the statistics of droplet splitting, we recorded images with 12 light exposures that showed the trajectories of single droplets (Extended Data Fig. 1b). Compared with larger droplets[6,7], we observed smaller deformations, a larger number of spicules with smaller relative sizes and higher fragment velocities (Extended Data Fig. 1c–f).

The stochastic nature of nucleation limits the time resolution to the spread of nucleation times, both in experiments using one-shot measurements of single drops[11,21] and in experiments examining several drops simultaneously, such as emulsion systems[8,9]. We addressed this problem by developing a detailed model for the freezing of a supercooled droplet. The model, illustrated in Fig. 2a, has seven optically identifiable stages of freezing. (1) Liquid supercooled water in which ice

Fig. 1 | Capturing the earliest stages of freezing in supercooled water drops. Water drops with a 40-μm diameter were injected into a vacuum chamber, in which they cooled rapidly and froze after homogeneous ice nucleation. Single freezing drops were examined using simultaneous X-ray laser diffraction and two-pulse optical imaging. Figure adapted from ref. 34, Springer Nature Ltd.

will nucleate homogenously. (2) Dendritic growth of ice, which freezes approximately half of the liquid[22] and deforms the droplet slightly. (3) An initial stage of inward freezing, in which a smooth solid shell of ice

forms around a core filled with a mixture of ice dendrites and liquid. (4) The appearance and growth of small spicules on the surface of the drop. The spicules are formed by liquid driven from the core through cracks in the solid shell, owing to the pressure build-up caused by the expansion of water on freezing. (5) Drops with large spicules. (6) Drops that cracked because of the pressure build-up but did not split. (7) Drops split into fragments. During freezing, the drops first evolve from stage 1 to stage 5, then freezing ends with one of stages 5, 6 or 7.

The freezing model is stochastic and was used to simulate freezing in large ensembles of drops. The ensemble simulations provided the probabilities of observing each freezing stage at a given time of flight, the probability of drops splitting over a range of times of flight, and ensemble-averaged properties, such as the time elapsed from nucleation.

The freezing-model parameters were determined using a complex fitting procedure (Methods and Supplementary Information). They are shown in Extended Data Table 1 and represent the best match between the model and our experiment, which is illustrated in Fig. 2b by comparing measured and modelled probabilities. Because the freezing parameters are implicitly dependent on the model, they are not a unique solution to the problem of quantifying all freezing stages, but the ice-nucleation rate and the dendrite-growth velocity are consistent with previous dedicated measurements (Methods and Extended Data Fig. 5), whereas the other parameters quantify further freezing processes.

The parameters of the freezing stages after the completion of dendritic growth are specific to our drop size, temperature and cooling rate. We modelled the durations of pressure build-up before the generation of spicules and the initial growth of spicules with fixed times, because the fit of the model was not improved when using normally distributed values. The fixed duration of stages 3 and 4 is consistent with both being approximately deterministic. By contrast, the fit of
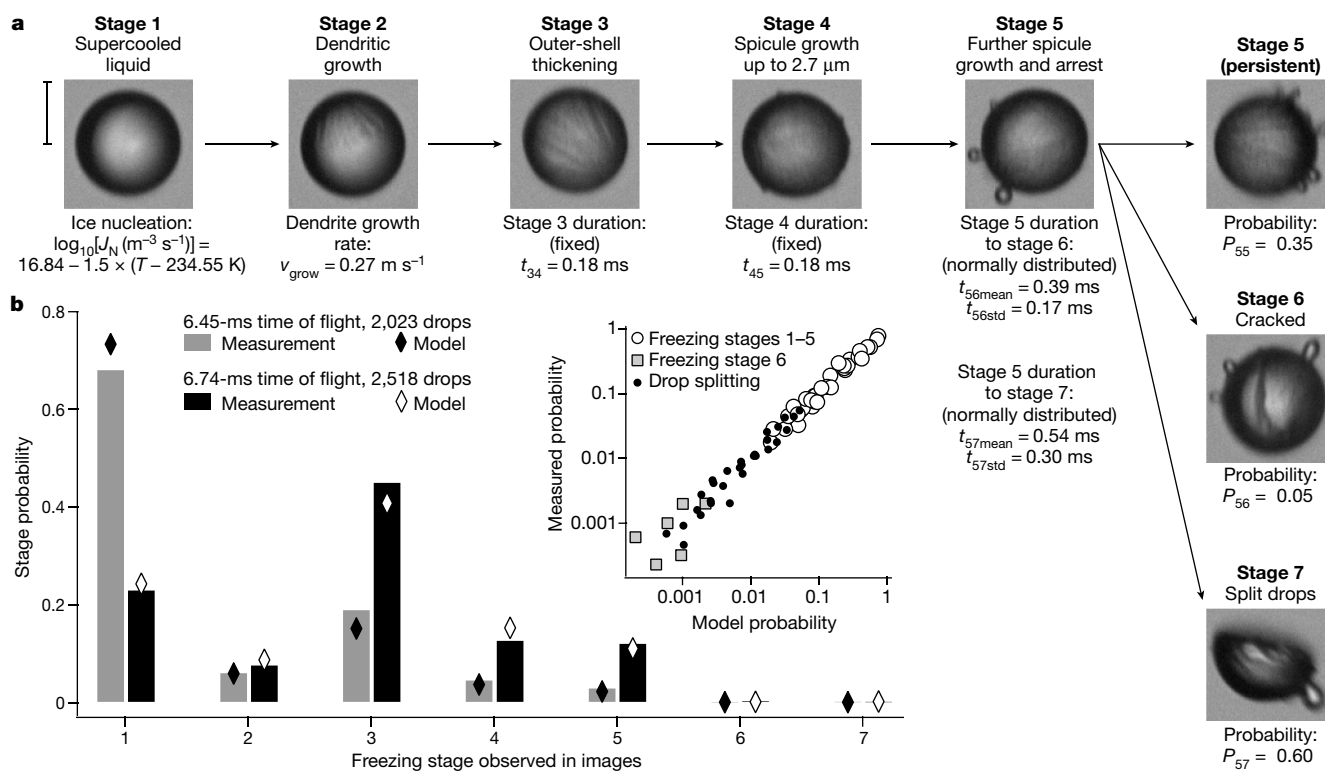
Fig. 2 | A detailed model of freezing in 40-μm supercooled water drops in vacuum, after homogeneous nucleation. a, The freezing process was modelled using seven stages of freezing that are identifiable in optical images. The dynamics of each stage is characterized by the physical parameters shown in the figure, which were obtained by fitting the model against measurements from thousands of drops. Scale bar, 25 μm. **b**, Comparison of experimental and modelled probabilities of observing drops in specific freezing stages. The graph shows the freezing-stage probabilities for two of the datasets and the inset shows the freezing-stage or the splitting probability for all the datasets used.

the model was better when using normally distributed values for the times spent before the fracture and splitting of drops, indicating that fracture and splitting are stochastic events.

In clouds, the splitting of frozen drops is a secondary ice-production process and its probability depends sensitively on the properties and environment of the drop[7,23]. The probability of splitting in our model, $P_{57} = 0.6$, is larger than those observed in experiments at atmospheric conditions[7], in which the duration of solidification is substantially longer (Methods and Extended Data Fig. 2i,j). Although P_{57} cannot be applied to cloud modelling, it is consistent with an observed increase of the splitting probability with the cooling rate[23], which could make it useful for parametrizing the splitting probability of cloud droplets. P_{57} is inconsistent with a model based on studying millimetre-sized drops freezing near 266 K, which predicted that drops with diameters less than 50 μm will not split[6]. This discrepancy can be explained by two factors that were different in our experiment: (1) the initial dendrites filled approximately half of the droplet volume and reinforced it against splitting and (2) according to our solidification model, the surface of drops cooled 14 degrees below the melting temperature at complete solidification (see Extended Data Fig. 2f), which would increase the fracture strength of ice. The increased fracture strength allows the build-up of more elastic energy before fragmentation and may restrict the pressure-releasing process of spicule growth.

The freezing model also enabled the calculation of the mean and standard deviation of the times elapsed from ice nucleation for all stages. For the earliest freezing stages, these standard deviations were approximately ±0.02 ms, shorter than the roughly 0.3 ms standard deviation of the nucleation times. Therefore, data sorted by the freezing stage had up to one order of magnitude better temporal resolution than unsorted data.

We analysed the evolution of X-ray scattering during freezing by grouping data from single drops by their freezing stage and by separating the crystal diffraction from liquid scattering (Extended Data Fig. 6 and Methods). Figure 3 and Extended Data Fig. 7 show representative scattering profiles from drops at different freezing stages.

The dominant changes in the X-ray scattering patterns during freezing were the increase of most crystal diffraction peaks relative to the first peak and the relative increase of the second liquid scattering peak. Most of the evolution of crystal diffraction patterns occurred before the drops reached stage 5 of freezing at approximately 0.5 ms after nucleation, indicating that long-range crystalline order formed on a timescale of less than a millisecond.

The scattering patterns from supercooled water drops had the same shape as observed previously, with the second liquid peak being higher than at the melting temperature[2]. During freezing, which heated the dendrite–liquid mixture close to the melting temperature, the second peak continued to increase, instead of becoming lower as expected for a heated bulk liquid. Because similar X-ray scattering patterns were observed from the quasi-liquid layer on the surface of premelted ice[19], it is probable that the interstitial liquid between the dendrites has a structure similar to the quasi-liquid layer on premelted ice and is related to the quasi-liquid layer between ice grains[20,24].

The crystal diffraction patterns showed all the main peaks characteristic of hexagonal ice. The relative heights of the peaks from drops in the last stages of freezing (Fig. 3 and Extended Data Fig. 7) were different from those observed in drops with annealed hexagonal ice[9]. Because the drops we investigated contain small crystals, peak heights different from bulk annealed ice are to be expected (Extended Data Fig. 7a). The raised background between the first three peaks is caused by diffraction spots from highly strained crystals (Extended Data Fig. 9). These spots are different from the features generated by stacking defects in X-ray laser diffraction[25]. The radial diffraction patterns did not show a notable signal near the cubic ice (400) peak at 3.93 Å⁻¹, which is unique to cubic ice and well separated from the nearest peaks of hexagonal
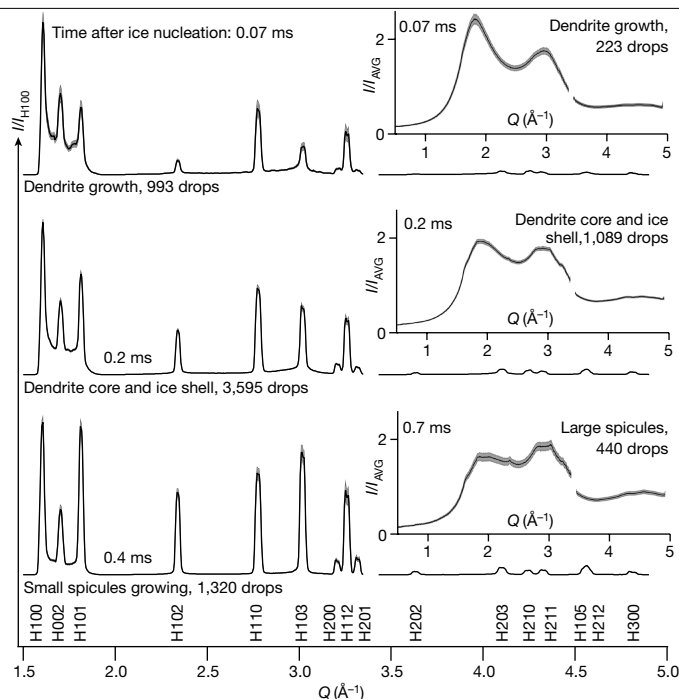

Fig. 3 | The evolution of X-ray scattering from the crystal and liquid phases during freezing. The crystal diffraction peaks (left), labelled according to the Miller indices of hexagonal ice, are characteristic of hexagonal ice. The intensity (I) of high-index reflections increases with the time elapsed after ice nucleation, indicating the formation of long-range crystalline order. The diffuse scattering patterns from the liquid (right) show a relative increase in the second diffuse peak. During freezing, the liquid scattering patterns become similar to those observed on premelted ice. The crystal data are normalized to the height of the first peak and the liquid data are normalized to the average intensity. The gap at 3.4 Å⁻¹ is a region with unreliable data near the edge of the attenuator shadow, which hides a hexagonal (004) peak. The standard deviations, evaluated by means of bootstrapping over bands with $\Delta Q = 0.0025$ Å⁻¹, are shown as upper and lower confidence bands at one standard deviation (Methods).

ice. We therefore conclude that, from 0.03 to 1 ms after freezing, the ice had a predominantly hexagonal structure.

This freshly formed ice is different from the stable hexagonal ice. Figure 4a shows an image of the X-ray detector data accumulated from stage 5 drops. As the diffraction angle increases, the diffraction peaks have increasingly elongated shapes in the radial direction, indicating a substantial inhomogeneous strain. Some of the peaks are also split, suggesting the existence of two preferred strain levels. A Williamson–Hall plot[26] is shown in Fig. 4b for drops in stages 4 to 7 examined at low intensity to prevent saturation. Further evaluations of the inhomogeneous strain for the crystal data shown in Fig. 3, which was affected by detector saturation (Methods), did not reveal a substantial evolution of the strain with the freezing stage; the strain remained large up to 1 ms after freezing and was not relaxed by the splitting of drops.

The evolution of the diffraction patterns during freezing indicates how the long-range crystalline order develops. At the shortest time delay investigated (27 μs on average; see Extended Data Fig. 7a), the diffraction was dominated by the (100), (110) and (002) peaks, which are the markers of short-range order in the (001) basal plane sheets and in the stacking distance of these sheets; the (101) peak, which is a marker of proper registration between sheets, had a low intensity. During freezing, both the peaks reflecting long-range order in the hexagonal sheets ((hk0), $h > 1$ or $k > 1$) and the peaks reflecting the registration of sheets (($h0l$), (hkl)) increased, with similar timescales. These observations indicate that the formation of crystalline order starts with short-range order in the basal plane sheets and in their stacking separation, and

Article
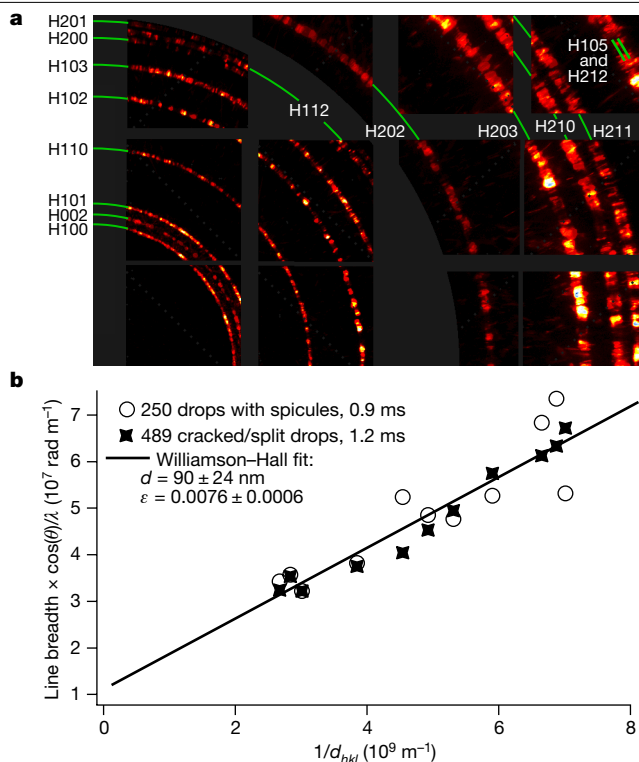
Fig. 4 | Inhomogeneous strain in rapidly solidified ice. a, Composite X-ray detector image showing the crystal diffraction accumulated from 784 drops in stage 5 of freezing, 0.7 ms on average after nucleation. The Bragg peaks are elongated in the radial direction and the elongation increases with the diffraction angle. **b**, The dependence of the broadening of crystal peaks on the reciprocal of the lattice planes spacing. The linear fit is a Williamson–Hall analysis providing the ice crystal grain size d and the inhomogeneous strain ε, with uncertainties calculated from the standard deviation of the fit coefficients.

then continues with a concurrent enhancement of the order within the sheets and in the registration of the sheets.

We investigated higher nucleation temperatures using drops that nucleated ice heterogeneously, doped with either Arizona Test Dust (ATD, nucleation at 240–249 K) or silver iodide (AgI, nucleation at 260–265 K). The same freezing stages were observed and their properties depended on temperature (see Supplementary Information and Extended Data Fig. 8c). The X-ray diffraction evolved with the freezing stage and Extended Data Figs. 8 and 9 compare the diffraction from pure and doped drops, for stages 2 and 5. In all cases, the diffraction profiles were consistent with the strained hexagonal ice structure and the similar widths of the peaks indicated a similar degree of strain.

The diffraction patterns after heterogeneous nucleation had higher peak heights during dendritic freezing, which can be explained by longer time delays after nucleation, but also suggests that the crystalline order develops faster and better in less supercooled drops. In particular, the drops with AgI showed the very weak hexagonal (104) peak and the raised background between the first three peaks was negligible. The diffraction images for drops with AgI (Extended Data Fig. 9) showed a combination of diffuse spots with bright spots with a smaller radial elongation, indicating that some crystals had a narrower strain distribution than the crystals grown in colder drops.

The strained hexagonal ice is the structure with long-range order that forms first in water microdrops supercooled by about 10 K to around 40 K. The existence of strained hexagonal ice at several nucleation temperatures indicates that this ice is probably a metastable state that precedes the formation of ice with stacking defects and high cubicity.

A transition from strained hexagonal ice to ice with stacking defects seems feasible energetically (Methods). Such an evolution of ice was discussed theoretically[27] but was not observed in simulations[28,29]. Experiments that observed ice with stacking defects in microdrops used concentrated emulsions[8,9,18,30]. On the basis of the applied cooling rates[30], the emulsions were examined minutes after freezing and spent seconds within a few degrees of the freezing temperatures. These time delays are much longer than in our experiment and may enable a transformation from strained hexagonal ice to ice with stacking defects. Here we did not observe an evolution towards the diffraction patterns of ice with stacking defects. Understanding how the strained hexagonal ice is related to ice with stacking defects will require further experiments that control the temperature of ice during and after freezing.

The freezing of supercooled water droplets is a complex sequence of processes. At the droplet scale, the complexity of freezing can be disentangled using large numbers of observations in combination with detailed physical modelling. This detailed quantification of freezing stages enables improved hydrodynamic models of drop freezing[6], which may become accurate enough to predict splitting probabilities and other properties relevant to secondary ice production in the atmosphere. At the molecular scale, the ice formed from supercooled water microdrops between 234 and 265 K evolves through possibly more than one class of metastable states before becoming a perfect crystal. A similarly rich freezing dynamics may occur in other substances, offering opportunities to understand non-equilibrium solidification and to discover metastable materials.

Online content

Any methods, additional references, Nature Portfolio reporting summaries, source data, extended data, supplementary information, acknowledgements, peer review information; details of author contributions and competing interests; and statements of data and code availability are available at https://doi.org/10.1038/s41586-023-06283-2.

1. Angell, C. A., Oguni, M. & Sichina, W. J. Heat capacity of water at extremes of supercooling and superheating. *J. Phys. Chem.* **86**, 998–1002 (1982).
2. Sellberg, J. A. et al. Ultrafast X-ray probing of water structure below the homogeneous ice nucleation temperature. *Nature* **510**, 381–384 (2014).
3. Stöckel, P., Weidinger, I. M., Baumgärtel, H. & Leisner, T. Rates of homogeneous ice nucleation in levitated H₂O and D₂O droplets. *J. Phys. Chem. A* **109**, 2540–2546 (2005).
4. Stan, C. A. et al. A microfluidic apparatus for the study of ice nucleation in supercooled water drops. *Lab Chip* **9**, 2293–2305 (2009).
5. Hagen, D. E., Anderson, R. J. & Kassner, J. L. Homogeneous condensation–freezing nucleation rate measurements for small water droplets in an expansion cloud chamber. *J. Atmos. Sci.* **38**, 1236–1243 (1981).
6. Wildeman, S., Sterl, S., Sun, C. & Lohse, D. Fast dynamics of water droplets freezing from the outside in. *Phys. Rev. Lett.* **118**, 084101 (2017).
7. Lauber, A., Kiselev, A., Pander, T., Handmann, P. & Leisner, T. Secondary ice formation during freezing of levitated droplets. *J. Atmos. Sci.* **75**, 2815–2826 (2018).
8. Murray, B. J., Knopf, D. A. & Bertram, A. K. The formation of cubic ice under conditions relevant to Earth's atmosphere. *Nature* **434**, 202–205 (2005).
9. Malkin, T. L., Murray, B. J., Brukhno, A. V., Anwar, J. & Salzmann, C. G. Structure of ice crystallized from supercooled water. *Proc. Natl Acad. Sci. USA* **109**, 1041–1045 (2012).
10. Buttersack, T. & Bauerecker, S. Critical radius of supercooled water droplets: on the transition toward dendritic freezing. *J. Phys. Chem. B* **120**, 504–512 (2016).
11. Esmaeildoost, N. et al. Heterogeneous ice growth in micron-sized water droplets due to spontaneous freezing. *Crystals* **12**, 65 (2022).
12. Pruppacher, H. R. & Klett, J. D. *Microphysics of Clouds and Precipitation* (Springer, 2010).
13. Murray, B. J., Carslaw, K. S. & Field, P. R. Opinion: Cloud-phase climate feedback and the importance of ice-nucleating particles. *Atmos. Chem. Phys.* **21**, 665–679 (2021).
14. Korolev, A. & Leisner, T. Review of experimental studies of secondary ice production. *Atmos. Chem. Phys.* **20**, 11767–11797 (2020).
15. Field, P. et al. Secondary ice production: current state of the science and recommendations for the future. *Meteorol. Monogr.* **58**, 7.1–7.20 (2017).
16. Kleinheins, J., Kiselev, A., Keinert, A., Kind, M. & Leisner, T. Thermal imaging of freezing drizzle droplets: pressure release events as a source of secondary ice particles. *J. Atmos. Sci.* **78**, 1703–1713 (2021).
17. Korolev, A. et al. Observation of secondary ice production in clouds at low temperatures. *Atmos. Chem. Phys.* **22**, 13103–13113 (2022).
18. Malkin, T. L. et al. Stacking disorder in ice I. *Phys. Chem. Chem. Phys.* **17**, 60–76 (2015).
19. Maruyama, M. et al. X-ray analysis of the structure of premelted layers at ice interfaces. *Jpn. J. Appl. Phys.* **39**, 6696–6699 (2000).

20. Dash, J. G., Rempel, A. W. & Wettlaufer, J. S. The physics of premelted ice and its geophysical consequences. *Rev. Mod. Phys.* **78**, 695–741 (2006).

21. Laksmono, H. et al. Anomalous behavior of the homogeneous ice nucleation rate in "no-man's land". *J. Phys. Chem. Lett.* **6**, 2826–2832 (2015).

22. Buttersack, T., Weiss, V. C. & Bauerecker, S. Hypercooling temperature of water is about 100 K higher than calculated before. *J. Phys. Chem. Lett.* **9**, 471–475 (2018).

23. Keinert, A., Spannagel, D., Leisner, T. & Kiselev, A. Secondary ice production upon freezing of freely falling drizzle droplets. *J. Atmos. Sci.* **77**, 2959–2967 (2020).

24. Thomson, E. S., Hansen-Goos, H., Wettlaufer, J. S. & Wilen, L. A. Grain boundary melting in ice. *J. Chem. Phys.* **138**, 124707 (2013).

25. Niozu, A. et al. Crystallization kinetics of atomic crystals revealed by a single-shot and single-particle X-ray diffraction experiment. *Proc. Natl Acad. Sci. USA* **118**, e2111747118 (2021).

26. Williamson, G. K. & Hall, W. H. X-ray line broadening from filed aluminium and wolfram. *Acta Metall.* **1**, 22–31 (1953).

27. Hondoh, T. Dislocation mechanism for transformation between cubic ice I_c and hexagonal ice I_h. *Philos. Mag.* **95**, 3590–3620 (2015).

28. Haji-Akbari, A. & Debenedetti, P. G. Direct calculation of ice homogeneous nucleation rate for a molecular model of water. *Proc. Natl Acad. Sci. USA* **112**, 10582–10588 (2015).

29. Lupi, L. et al. Role of stacking disorder in ice nucleation. *Nature* **551**, 218–222 (2017).

30. Murray, B. J. & Bertram, A. K. Formation and stability of cubic ice in water droplets. *Phys. Chem. Chem. Phys.* **8**, 186–192 (2006).

Article

Methods

The experiments were conducted at the Coherent X-ray Imaging (CXI) instrument[31] of the Linac Coherent Light Source (LCLS) X-ray free-electron laser (XFEL) facility[32]. The experimental set-up was installed in the SC1 sample environment set-up, which provided a vacuum environment with a pressure below 0.1 Pa. SC1 included X-ray optics that focused the XFEL pulses to a nominal diameter of 1 μm and a Cornell-SLAC pixel array detector (CSPAD) X-ray camera[33] to record scattering and diffraction from single XFEL pulses interacting with the droplets.

Droplet generation

Droplets of ultrapure water (Milli-Q Integral, MilliporeSigma) and of water with ice-nucleating particles were generated using a 20-μm-diameter glass nozzle equipped with a piezoelectric actuator (MJ-AT series, MicroFab Technologies). To maximize the data-collection rate, the droplet-generation parameters were adjusted during experiments. The drop diameter and velocities used in the data analysis were measured for each data group having the same generation parameters. The nozzle had a pressure differential of 1.6–1.9 bar and a flow rate of 11.3–12 ml h^{-1}, and the piezoelectric actuator was driven by a 69-kHz sinusoidal voltage with 16–20 V peak-to-peak amplitude. The droplets had an initial temperature of 292 K, diameters ranging from 40.0 to 44.7 μm when examined and velocities ranging from 16.0 to 18.1 m s^{-1}.

Samples for heterogeneous nucleation

For ATD-doped drops, 4.91 g of ATD (grade A1 Ultrafine, Reade Advanced Materials) were mixed in a glass vial with 44.2 ml of ultrapure water, sonicated and left to settle for 6 h. 11 ml of clear suspension were collected from the top of the vial, diluted ten times with ultrapure water and then used to generate the drops. For AgI-doped drops, a colloidal solution with 1 mM concentration of AgI was prepared as described previously[4]. The colloidal solution was then diluted 50 times with ultrapure water and used to generate the drops. The particle sizes, determined with a nanoparticle tracking analyser (NanoSight, Malvern Panalytical), were 0.3 ± 0.1 μm for ATD and 0.15 ± 0.05 μm for AgI, and their concentration was on the order of 100 particles per drop for both samples.

Optical imaging

The optical imaging system was similar to that described in ref. 34 except for (1) using only the right-angle imaging path and setting it perpendicular to the XFEL beam and (2) using a different illumination source that used several light pulses to characterize the kinematics of drops and split fragments[35]. A pulsed LED illuminator (IL-106B, HARDsoft Microprocessor Systems) generated 200-ns blue light pulses (460 nm) at 200 kHz repetition rate. The illuminator had a much higher repetition rate than the XFEL (120 Hz) and produced trains of light pulses that were synchronized with each of the XFEL pulses.

Two different microscope objectives (long-working-distance apochromats, Mitutoyo) were used. A 20× objective was used for the primary two-exposure data, producing images with a magnification of 497 nm pixel^{-1} and a resolution better than 780 nm. A 2× objective was used for the secondary 12-exposure data, producing images with a magnification of 5.1 μm pixel^{-1} and a resolution of 7.8 μm.

X-ray scattering and diffraction

The XFEL was operated in a self-amplified spontaneous emission mode and produced pulses with 40 fs duration, 9.5 keV photon energy and 3 mJ average pulse energy at the XFEL source. The estimated beamline transmission was 0.4 and the XFEL pulses were further attenuated by factors from 0.009 to 0.331 to prevent detector damage, with more attenuation needed at longer times of flight. This resulted in average pulse energies at the drops from 0.01 to 0.42 mJ.

An aluminium disc was used to attenuate the crystal diffraction at low angles, enabling the collection of weak X-ray scattering at high angles. The post-sample attenuator was a polycrystalline aluminium disc with a diameter of 74.9 mm and a thickness of 0.5 mm. For experiments with pure water, the X-ray detector and the post-sample attenuator were located approximately 70 mm and 43 mm, respectively, from the droplets. For heterogeneous nucleation experiments, these distances were 66 mm and 41 mm.

Processing of optical images

The intensity of images was rescaled linearly to correct the loss of contrast owing to the multiple exposures[36]. From approximately one million two-exposure images recorded, a subset of approximately 50,000 images that probably contains droplets was selected on the basis of the image intensities. This subset was investigated frame by frame and 20,580 images containing drops with identified freezing stages were found. The 12-exposure image data contained 10,855 images with approximately 34 drops per image; these images were investigated frame by frame to detect splitting events. Freezing-stage probabilities, splitting probabilities and further freezing statistics shown in Extended Data Fig. 1 were determined through manual measurements. The images used for analysis and the code for linear rescaling have been deposited at the CXIDB data repository[37].

Processing of X-ray scattering data

A detailed description of the X-ray data analysis is available in the Supplementary Information and the corresponding codes[38] are available at Zenodo. Only individual detector images that had a corresponding doubly exposed optical image of the droplet were used. The geometry of the X-ray detector was refined[39] using accumulated X-ray diffraction images from ice crystals. The raw detector data for pure water drops were corrected for background noise, common-mode noise and polarization, and the raw data for drops with AgI or ATD were corrected for background noise and polarization. These corrected detector data were separated at the pixel level into crystal diffraction from ice crystals and diffuse scattering from the liquid. The separated data were corrected for the post-sample attenuation and then grouped by the freezing stage of the drops and by the pulse energy at the sample, averaged across the data groups and integrated angularly to obtain the scattering intensities as a function of the photon momentum transfer. The absolute scattering cross-sections could not be determined because the scattered X-ray intensity depended on the X-ray pulse energy, the overlap of the droplet with the beam and the volumetric fraction of ice. Total, crystal and liquid scattering images were also assembled from the data groups by summation (see Fig. 4a and Extended Data Figs. 6a–c and 9).

The statistical uncertainties of the intensity values in the diffraction profiles were evaluated by means of bootstrapping. Single-shot diffraction profiles were sampled with replacement from the set of experimental profiles for a given freezing stage and then averaged into a test profile. The number of samples was equal to the number of experimental single-shot profiles and 10,000 test profiles were calculated. The mean and standard deviation of intensity at each Q point were calculated from the test profiles. Owing to the large number of test profiles, the bootstrapped mean is very close to the simple mean of single-shot data and is indistinguishable from it in the figures. The bootstrapped standard deviation did not change substantially when the Q bin size was increased several fold, because the bin size is a few times smaller than the size of the elongated diffraction spots. For ice in stages 2–5, the stage-to-stage peak height differences of the (101), (102), (110), (103) and (112) peaks, whose changes during freezing were most prominent, are larger than their standard deviations. Between hidden ice in stage 1 and ice in stage 2, (112) changed by more than the standard deviation, whereas the other four peaks changed by approximately the same as their standard deviation in stage 1.

We note that the diffraction measurements represent a compromise between the linearity of the detector data and the ability to record scattering intensities that have a wide dynamic range owing to the large difference in the diffracted intensities from the liquid and crystal phases. In some datasets, the first peak height may be underestimated owing to detector saturation, those from 2.7–3.4 Å may be affected by detector noise or the (200), (201) and (300) peaks may be undersampled because of the detector geometry.

Extended Data Fig. 7a compares an experimental diffraction pattern from drops in stages 4–7 with a simulated diffraction pattern from a cylinder of hexagonal ice with 100 nm diameter, 100 nm height and faces parallel to the basal plane. The simulation was performed using DIFFaX[40] v1.813, using the ice-crystal model given by Malkin et al.[9] with the unit cell dimensions at 0 °C, no stacking defects, no strain and scattering from oxygen atoms only. For an infinite crystal, this simulation reproduces the pattern given by Malkin et al.[9] for bulk ice. The peak heights simulated for the 100-nm ice cylinder are different and illustrate the impact of crystal size and shape. The simulated pattern in Extended Data Fig. 7a also includes the instrumental broadening, which was calculated from the raw pattern generated by DIFFaX, using the wavelength distribution of the XFEL pulses (Gaussian with 0.1% standard deviation).

Metastability of the strained hexagonal ice

Despite having the same basic crystal structure as the stable form of ice, the strained hexagonal ice has a higher energy that may allow transitions to other metastable forms of ice. The maximum elastic energy associated with the inhomogeneous strain, $K\varepsilon^2/2 \approx 5$ J mol^{-1}, in which $K = 8.5$ GPa is the bulk modulus of ice and $\varepsilon = 0.0076$ is the inhomogeneous strain from Fig. 4b, is on the same order of magnitude as the 8 J mol^{-1} energy needed to induce a high density of stacking defects[41]. Also, the stacking-defect energy is smaller than the energies that can be released through the annealing of crystal defects and interfaces[41]. Dendritic growth may be necessary for the formation of strained hexagonal ice, because water nanodrops, which are too small to form dendrites, freeze to ice with stacking defects and high cubicity within 100 μs of nucleation at approximately 50 K supercooling[42].

Models for evaporative cooling of liquid drops and spherically symmetric solidification of freezing drops

A detailed description of these models is available in the Supplementary Information and the corresponding codes[43] are available at Zenodo. The drops were assumed to be spherical during evaporation and solidification and their volume was divided into concentric spherical subshells. The evaporative cooling model (Extended Data Fig. 2a) computed the subshell temperatures by numerically solving heat equations that included the evaporative cooling at the surface and the thermal conduction inside the drop[44]. The solidification model (Extended Data Fig. 2b) tracked the inward growth of the solid ice shell. It advanced the freezing boundary by one subshell per time step and calculated the duration of the time steps to determine the shell growth towards the centre of the drop. The temperatures of fully frozen subshells were calculated by numerically solving heat equations that included cooling at the droplet surface, heat conduction in the fully frozen shell and heating at the freezing front owing to the release of latent heat. The duration of the time steps was obtained by equating, at the freezing front, the heat fluxes owing to thermal conduction in ice and owing to latent heat release.

The models used a Crank–Nicolson scheme[45] (see Extended Data Fig. 2c) to solve the heat equations efficiently. The numerical convergence of the models is illustrated in Extended Data Fig. 2d–f. The accuracy of the models was tested against experimental data[2,16,44,46,47] and analytical models[6] (see Extended Data Fig. 2g,h)

Three versions of the solidification model were developed to evaluate the time in which isolated drops with 1–100 μm radii solidify when

instantaneously exposed to vacuum, to air at atmospherically relevant conditions[48] (temperature, pressure and humidity) and to an oil matrix. The solidification times are shown in Extended Data Fig. 2i–k.

Seven-stage droplet-freezing model

A detailed description of the freezing model is given in the Supplementary Information and the corresponding codes[43] are available at Zenodo. The model was developed to be as simple as possible while providing a good match with the experimental data. For example, the model distinguishes between small and large spicules because the distributions of spicule heights at different times of flight (Extended Data Fig. 1d) indicated that the spicule growth occurred in spurts.

The freezing model tracks the droplet until it reaches the examined region; it assigns the time and location of nucleation, calculates the duration of each subsequent stage and assigns one of the terminal freezing stages (5, 6 or 7). The duration of stage 2 is determined by the dendritic-growth velocity. The duration of stages 3 and 4 is given by fixed times. The duration of stage 5 depends on the end stage: it is implicitly infinite if freezing ends in stage 5 and is given by normally distributed times if freezing ends in stages 6 or 7. The model was implemented numerically using subroutines for each of the stages. The subroutines calculate the end times of the freezing stages, which are stochastic values, and compare them with the time of flight. The simulation advances to the next stage if the end time is smaller than the time of flight or ends the calculation otherwise. The main outputs of the simulation are the freezing stage at a given time of flight and the time elapsed between nucleation and the time of flight. Both the actual stage of freezing and one that would be observed in an image are calculated, because they can be different (Extended Data Fig. 3c,d).

The statistical behaviour of the freezing simulation was verified by calculating the distribution of freezing stages and the standard deviation of drops in all freezing stages, using simulations of droplet ensembles. The distribution and their standard deviation of the number of drops in a stage are expected to have a binomial distribution. The droplet ensemble simulations were consistent with a binomial distribution, as shown in Extended Data Fig. 4a,b.

Ice-nucleation and dendritic-growth rates from the freezing model

The modelled ice-nucleation rate is shown in Extended Data Fig. 5a and applies to homogenous nucleation between 233.7 and 235.6 K. It is consistent with high-accuracy measurements at higher temperatures (235.4–237.9 K) on levitated[3] and microfluidic[4] drops, and with measurements at lower temperatures (226–232.5 K) on nanodrops[5,49]. The nucleation rate is also consistent with nucleation-rate parametrizations that use a Vogel–Fulcher–Tammann dependence of the self-diffusion coefficient of water[50–52]. The modelled nucleation rate is inconsistent with a smaller ice-nucleation rate measured between 229 and 232 K in another X-ray laser experiment on evaporatively cooled droplets, in which the droplet sizes and the times of flight were not measured in situ[21]. Because in that experiment the drops were not imaged optically during data collection, it was not possible to quantify phenomena that can affect the measurement of nucleation rates, such as the spread of the droplet stream[36] and variations of the droplet diameter and velocities.

The growth rate of dendritic ice, 0.27 m s^{-1} between 233.7 and 235.6 K, is nearly the same as the extrapolation of Pruppacher's data[53] for dendritic ice growth in drops below 264 K, but is inconsistent with a reported maximum in the ice-growth rate[10] near 255 K (Extended Data. Fig. 5b).

Determination of the parameters of the freezing model

A detailed description of this procedure is given in the Supplementary Information. The model has 11 primary freezing parameters and five auxiliary parameters (Extended Data Table 1). The freezing parameters

Article

were determined by fitting the freezing model against the experimental data. The fitting consisted in minimizing the difference between the measured and simulated probabilities of observed freezing stages in the two-exposure image data and between the measured and simulated splitting probabilities in the 12-exposure image data. This difference was quantified by an error function equal to the base-10 logarithm of the product of binomial probabilities of observing the measured numbers of droplets at the simulated probability. Codes for the calculation of the error function[43] are available at Zenodo. To reduce the statistical noise, the numerical freezing simulations were conducted at ten times the number of experimentally measured drops and the determination of all freezing parameters required approximately one billion single-droplet simulations.

The error function depends on the parameters of the freezing model through the simulated probabilities. The error function has a stochastic output and was minimized in two steps. First, on the order of 1,000 error function values were sampled near its minimum using a pattern search algorithm[54]. The sampled values were then fitted with a multi-dimensional parabolic function to improve the precision of the freezing parameters at the minimum of the error function. For part of the parameters, the minimum was refined further using single-parameter scans of the error function followed by fitting with parabolic functions. The minimization procedure was applied sequentially using either the two-exposure or the 12-exposure data to determine the freezing parameters that were most sensitive to that part of the experimental data.

The overall validity of the parameter-optimization procedure was tested by comparing the experimental and simulated numbers of split fragments observed in the two-exposure data, which were not used for the optimization procedure. The model predicts fragment numbers consistent with the experiment within the statistical fluctuations (see Extended Data Fig. 4f).

The statistical uncertainty of the freezing parameters (see Extended Data Table 1) was calculated as the change in the value of the parameter that led to a one-standard-deviation increase in the error function, along the parabolic fit function that was used to determine the minimum. The standard deviation of the error function was estimated as the standard deviation of the error function when the simulation was run with the same number of drops as in the experiment.

All numerical models and the determination of the freezing parameters were implemented as codes in MATLAB R2022a. The numerical calculations were performed on a Lenovo P620 workstation with a 64-core AMD Threadripper PRO 3995WX processor and 128 GB of RAM.

Data availability

All optical image and X-ray scattering data used in this study have been deposited[37] at the CXIDB repository. Source data are provided with this paper.

Code availability

Codes for modelling cooling, solidification and staged freezing[43] and for processing the X-ray data[38] are available at Zenodo. Codes for extracting the optical images and X-ray scattering data have been deposited[37] at the CXIDB repository, along with the data.

31. Liang, M. N. et al. The coherent X-ray imaging instrument at the Linac Coherent Light Source. *J. Synchrotron Radiat.* **22**, 514–519 (2015).
32. Emma, P. et al. First lasing and operation of an ångstrom-wavelength free-electron laser. *Nat. Photonics* **4**, 641–647 (2010).
33. Hart, P. et al. The CSPAD megapixel x-ray camera at LCLS. *Proc. SPIE* **8504**, 51–61 (2012).
34. Stan, C. A. et al. Liquid explosions induced by X-ray laser pulses. *Nat. Phys.* **12**, 966–971 (2016).
35. Brownscombe, J. & Thorndike, N. Freezing and shattering of water droplets in free fall. *Nature* **220**, 687–689 (1968).
36. Stan, C. A. et al. Rocket drops: the self-propulsion of supercooled freezing drops. *Phys. Rev. Fluids* **8**, L021601 (2023).
37. Kalita, A. X-ray laser diffraction and optical image data from freezing supercooled water drops. CXIDB ID 217. *CXIDB* https://doi.org/10.11577/1973475 (2023).
38. Stan, C. A., Marte, S., Kalita, A. & Mrozek-McCourt, M. Separation of sharp and diffuse diffraction patterns from X-ray laser scattering of freezing water drops. Version 1.0. *Zenodo* https://doi.org/10.5281/zenodo.7908740 (2023).
39. Yefanov, O. et al. Accurate determination of segmented X-ray detector geometry. *Opt. Express* **23**, 28459–28470 (2015).
40. Treacy, M., Newsam, J. & Deem, M. A general recursion method for calculating diffracted intensities from crystals containing planar faults. *Proc. R. Soc. Lond. A* **433**, 499–520 (1991).
41. Hudait, A., Qiu, S. W., Lupi, L. & Molinero, V. Free energy contributions and structural characterization of stacking disordered ices. *Phys. Chem. Chem. Phys.* **18**, 9544–9553 (2016).
42. Amaya, A. J. et al. How cubic can ice be? *J. Phys. Chem. Lett.* **8**, 3216–3222 (2017).
43. Stan, C. A., Kalita, A. & Mrozek-McCourt, M. Modeling of supercooling, solidification, and freezing stages of water drops. Version 1.0. *Zenodo* https://doi.org/10.5281/zenodo.7908648 (2023).
44. Smith, J. D., Cappa, C. D., Drisdell, W. S., Cohen, R. C. & Saykally, R. J. Raman thermometry measurements of free evaporation from liquid water droplets. *J. Am. Chem. Soc.* **128**, 12892–12898 (2006).
45. Crank, J. & Nicolson, P. A practical method for numerical evaluation of solutions of partial differential equations of the heat-conduction type. *Math. Proc. Camb. Philos. Soc.* **43**, 50–67 (1947).
46. Goy, C. et al. Shrinking of rapidly evaporating water microdroplets reveals their extreme supercooling. *Phys. Rev. Lett.* **120**, 015501 (2018).
47. Ando, K., Arakawa, M. & Terasaki, A. Freezing of micrometer-sized liquid droplets of pure water evaporatively cooled in a vacuum. *Phys. Chem. Chem. Phys.* **20**, 28435–28444 (2018).
48. Rosenfeld, D. & Woodley, W. L. Deep convective clouds with sustained supercooled liquid water down to -37.5 °C. *Nature* **405**, 440–442 (2000).
49. Amaya, A. J. & Wyslouzil, B. E. Ice nucleation rates near ~225 K. *J. Chem. Phys.* **148**, 084501 (2018).
50. Zobrist, B., Koop, T., Luo, B., Marcolli, C. & Peter, T. Heterogeneous ice nucleation rate coefficient of water droplets coated by a nonadecanol monolayer. *J. Phys. Chem. C* **111**, 2149–2155 (2007).
51. Ickes, L., Welti, A., Hoose, C. & Lohmann, U. Classical nucleation theory of homogeneous freezing of water: thermodynamic and kinetic parameters. *Phys. Chem. Chem. Phys.* **17**, 5514–5537 (2015).
52. Koop, T. & Murray, B. J. A physically constrained classical description of the homogeneous nucleation of ice in water. *J. Chem. Phys.* **145**, 211915 (2016).
53. Pruppacher, H. R. Interpretation of experimentally determined growth rates of ice crystals in supercooled water. *J. Chem. Phys.* **47**, 1807–1813 (1967).
54. Hooke, R. & Jeeves, T. A. "Direct search" solution of numerical and statistical problems. *J. ACM* **8**, 212–229 (1961).

Author contributions C.A.S. conceived and designed the study. C.A.S., S.B., P.R.W., J.E.K., M.J.H., R.H.P. and S.A.H.G. prepared the experiment. C.A.S., P.R.W., N.D.L., R.G.S., H.L., A.L.A., M.L. and S.B. conducted the experiment. T.F.K., M.M.-M., A.K., S.M. and C.A.S. analysed the optical image data. C.A.S., S.M., M.M.-M., A.K. and N.D.L. analysed the X-ray scattering data. A.K., M.M.-M. and C.A.S. developed the models and determined the freezing parameters. C.A.S. wrote the manuscript.
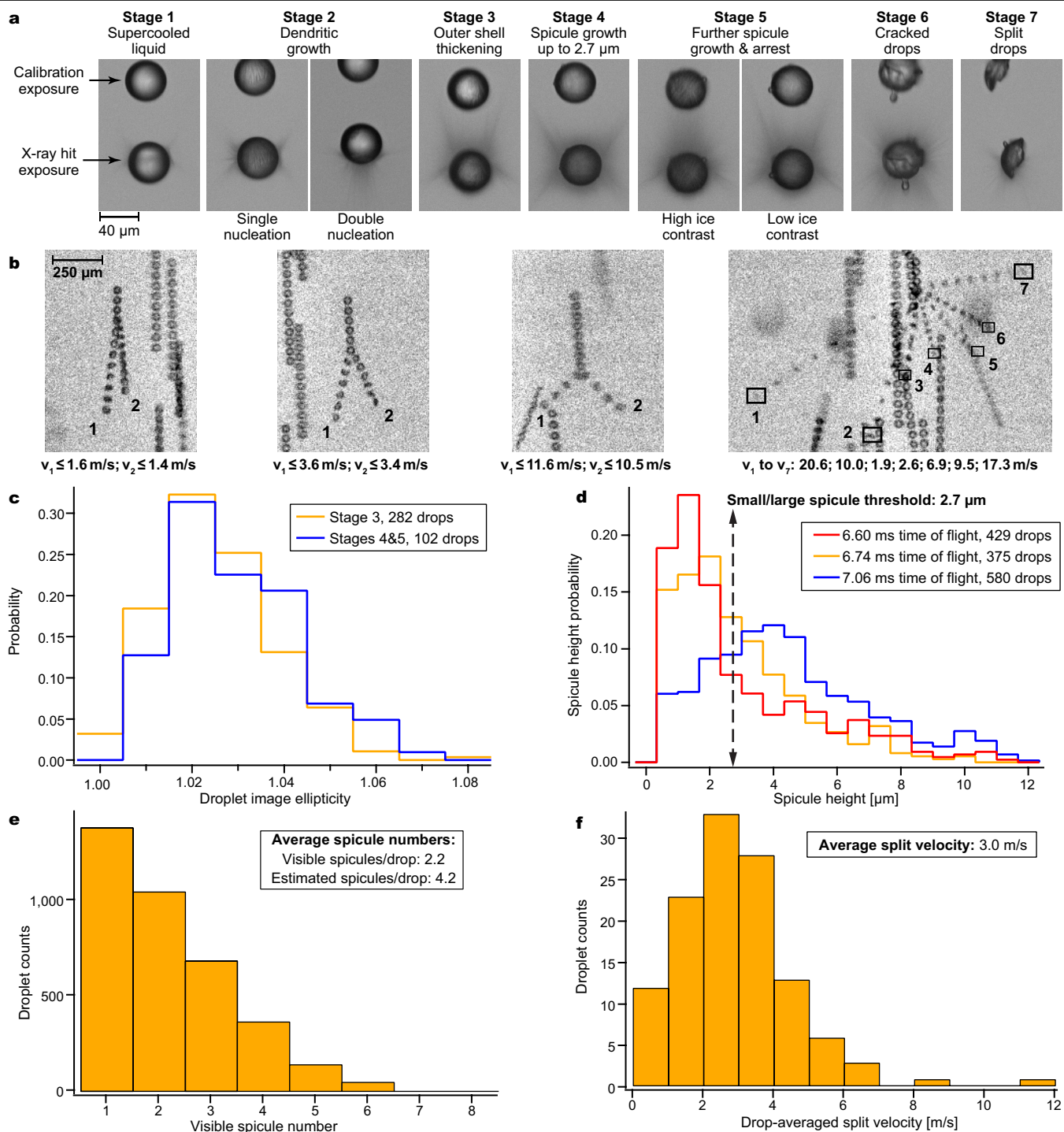
Extended Data Fig. 1 | Optical imaging and characterization of freezing processes. a, Drops at different stages of freezing. The images show two exposures of the same drop, with the second (lower) exposure capturing the blowup resulting from the XFEL pulse. The droplets travelled from top to bottom in the images. **b**, Drop-splitting events captured using 12 exposures for each drop. The images illustrate the range of fragment velocities in binary fractures and a seven-fragment fracture. The velocities measured from images may be smaller than the true velocity owing to translations perpendicular to the image plane. **c**, The ellipticity of droplet images indicates that the freezing-induced deformation is mostly complete before stage 3 of freezing. **d**, Evolution of the distribution of spicule heights with the time of flight. The distributions evolved discontinuously, justifying the distinction between small and large spicules. **e**, Distribution of visible spicule numbers. **f**, Distribution of fragment velocities after binary fractures. The histogram shows the geometric mean of the fragment velocities.
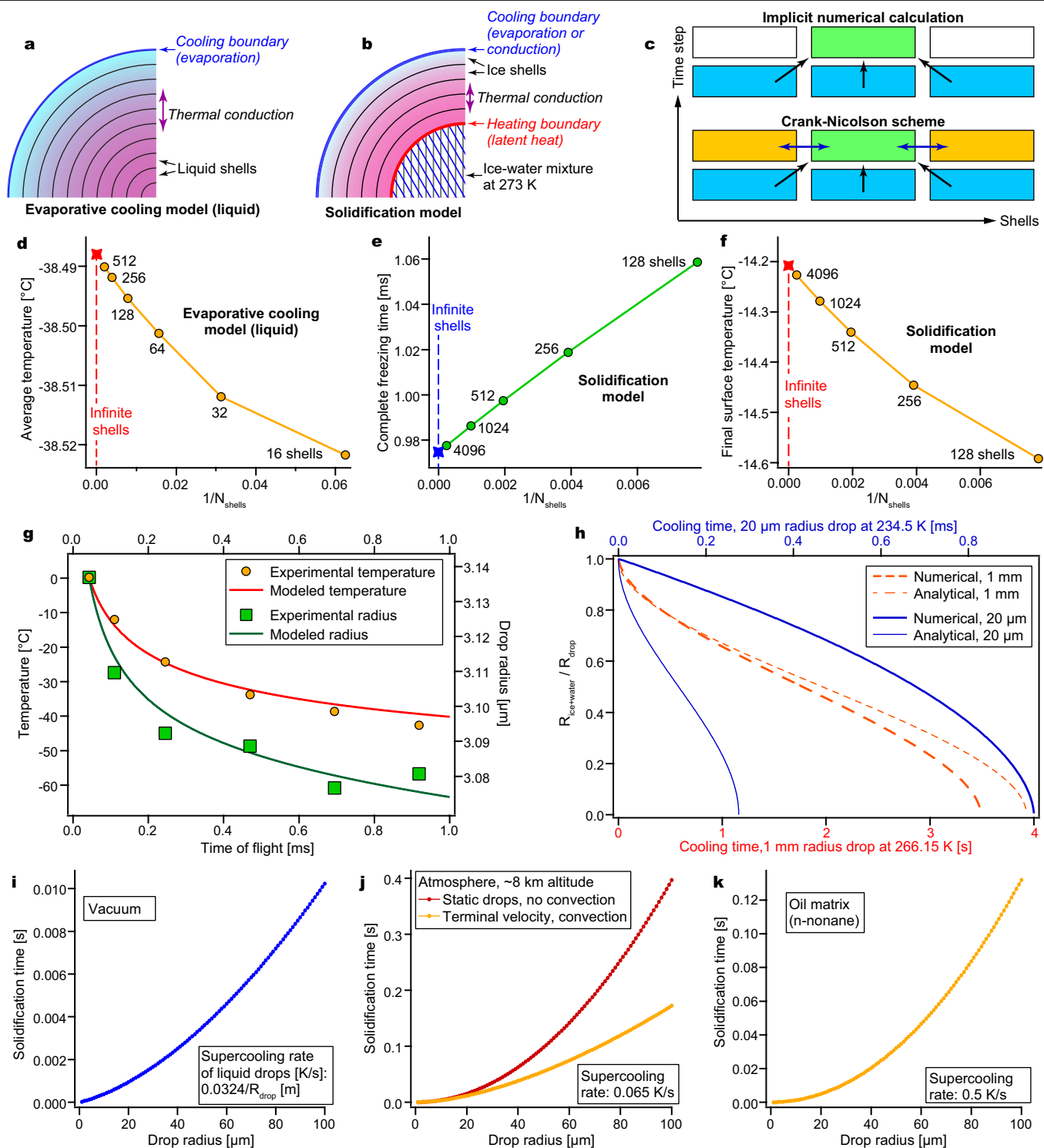
**Extended Data Fig. 2 | Evaporative cooling and coarse solidification models.**
a,b, Model geometries. **c,** Implicit and Crank–Nicolson schemes. **d–f,** The numerical convergence of the models. **g,** Comparison of the cooling model with the measurements of Goy et al.[46]. **h,** Comparison of the solidification model versus the analytical model of Wildeman et al.[6]. **i–k,** Modelled solidification times of an isolated 40.2-µm-diameter drop, after the completion of dendritic ice growth, in three scenarios: evaporative cooling in vacuum, atmospheric cooling of stationary and free-falling drops in a standard atmosphere at roughly 8 km altitude (236 K, 34 kPa) and cooling in an oil matrix.
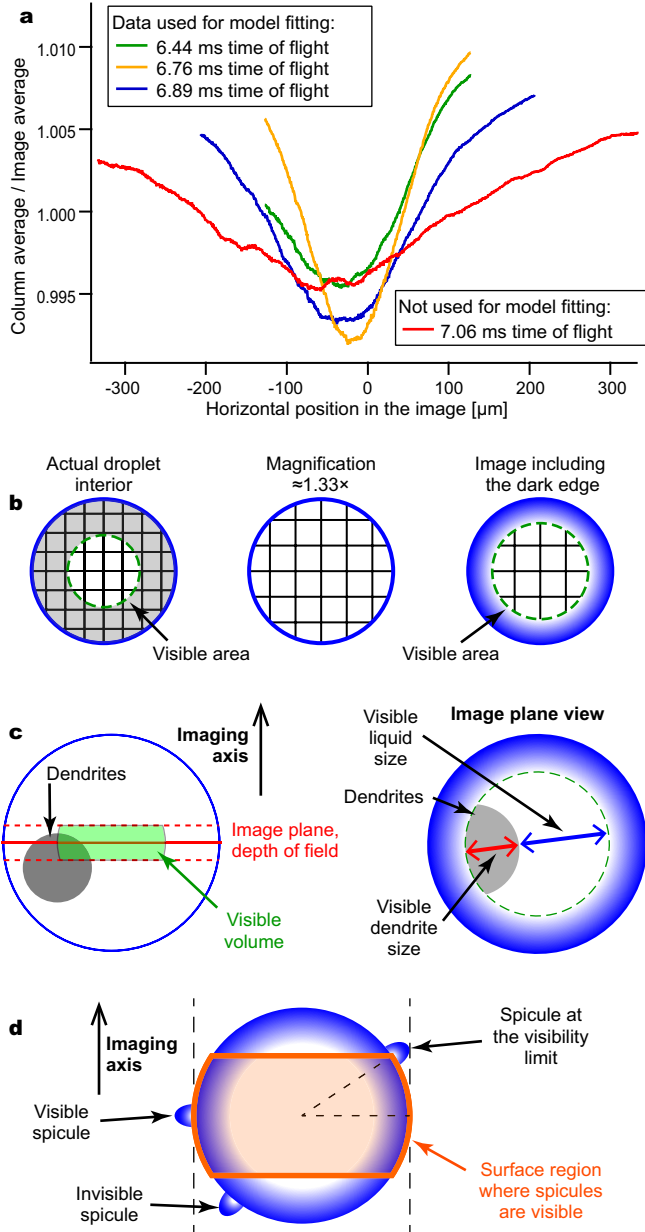
Extended Data Fig. 3 | Statistical and observational biases in the image data.
a, Vertically integrated image intensities for experiments with two optical
exposures, recorded at different times of flight. The image intensity decreases
as the number of drops observed at a given horizontal position increases.
Freezing leads to an increase in the lateral spread of the drops[36], which can
affect the stage statistics. To mitigate this statistical bias, only data up to
6.89 ms were used to determine the freezing parameters. **b**, Illustration
of the magnification of the image of the interior of the drop. **c**, Stage 2 of
freezing can be observed only if the ice region overlaps with the imaged volume
and its size in the image exceeds a minimum size. The liquid region must also
exceed this minimum size to identify stage 2 in a freezing drop. **d**, Spicules are
visible only if they extend outside the drop image. This is equivalent to the
spicules being visible only if they grew on a specific region of the drop surface.
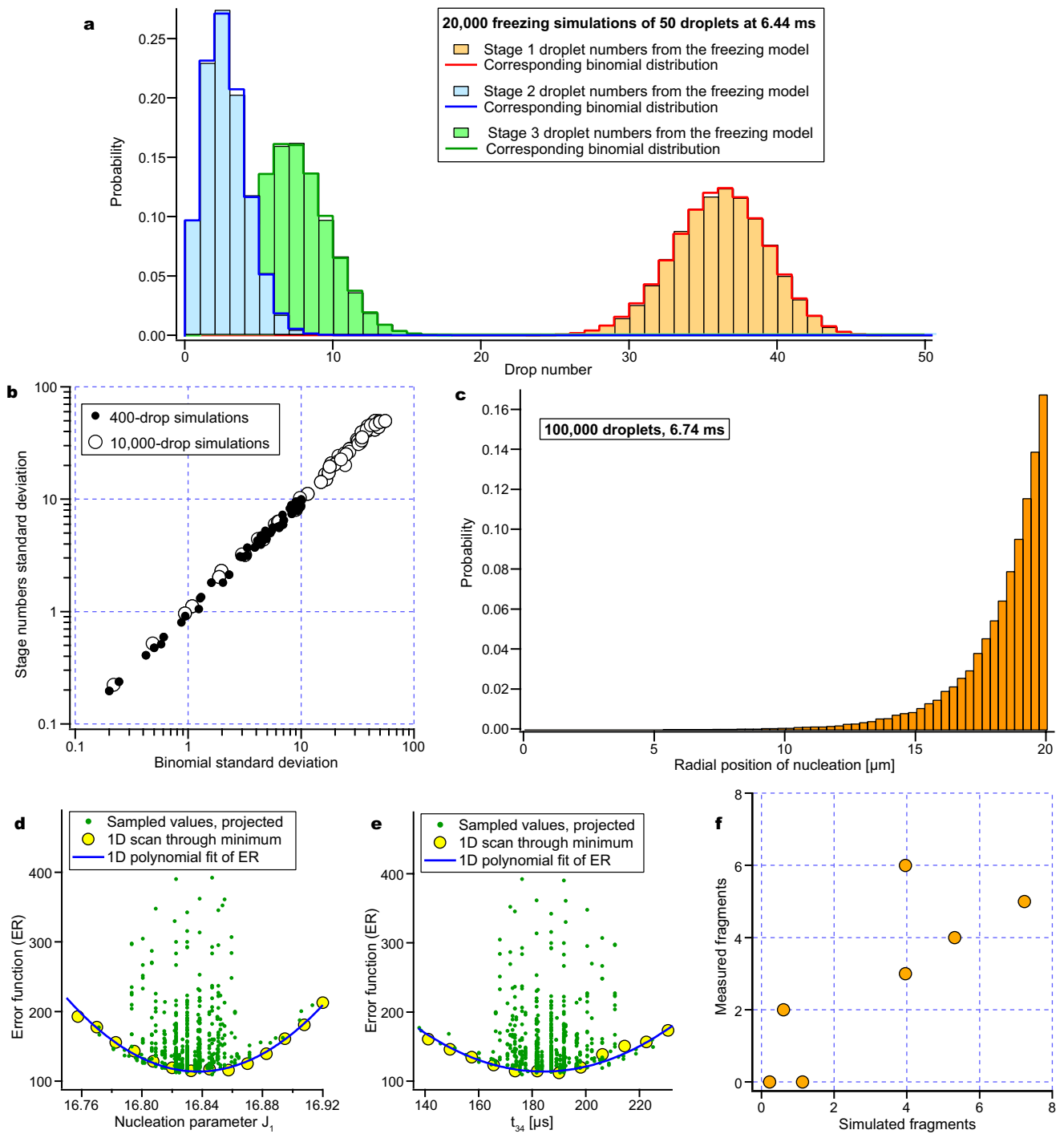
Extended Data Fig. 4 | Simulations of freezing drop ensembles and determination of the freezing parameters. a,b, Verification of the statistics of the ensemble simulations. The numbers of droplets observed in each stage have binomial distributions and the standard deviations of stage numbers are equal to the binomial standard deviations. **c,** The radial distribution of ice-nucleation events. **d,e,** Two-stage fitting of the parameters of the freezing model. Error-function values were sampled near the minimum using a pattern-search algorithm, then the error-function dependencies on the parameters were fitted with parabolic functions to find the minimum of the error function. **f,** Comparison of the numbers of drop fragments from experiments and simulations. The fragment numbers provide an independent test of the model because they were not used for the determination of the freezing parameters.
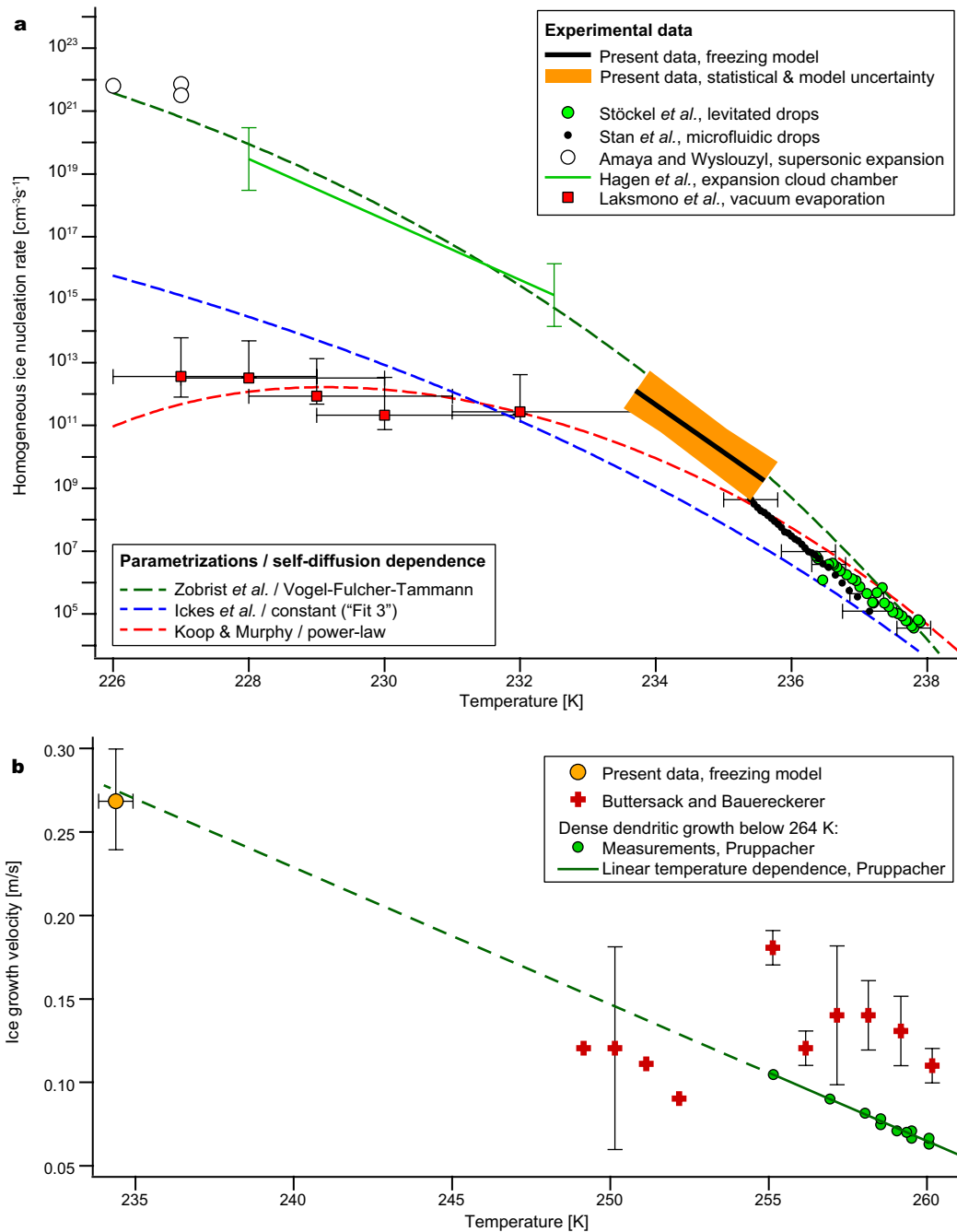
Extended Data Fig. 5 | Freezing-model results. a, The modelled ice-nucleation rate is a parametrization valid between 233.7 and 235.6 K. It is consistent with several other measurements at both lower and higher temperatures and with a parametrization based on a Vogel–Fulcher–Tammann temperature dependence of self-diffusion[50]. It is not consistent with another similar study conducted at an X-ray laser[21] or with parametrizations with constant[51] or power-law[52]

dependencies of the self-diffusion. **b**, The modelled dendritic ice growth velocity lies close to the extrapolation of Pruppacher's data[53] for the bulk growth of dense dendrites below 264 K, which scales linearly with the temperature. The error bars and bands represent the uncertainty of the freezing parameters (Extended Data Table 1) and of the temperature. For the literature data, the error bars are reproduced from the original work.
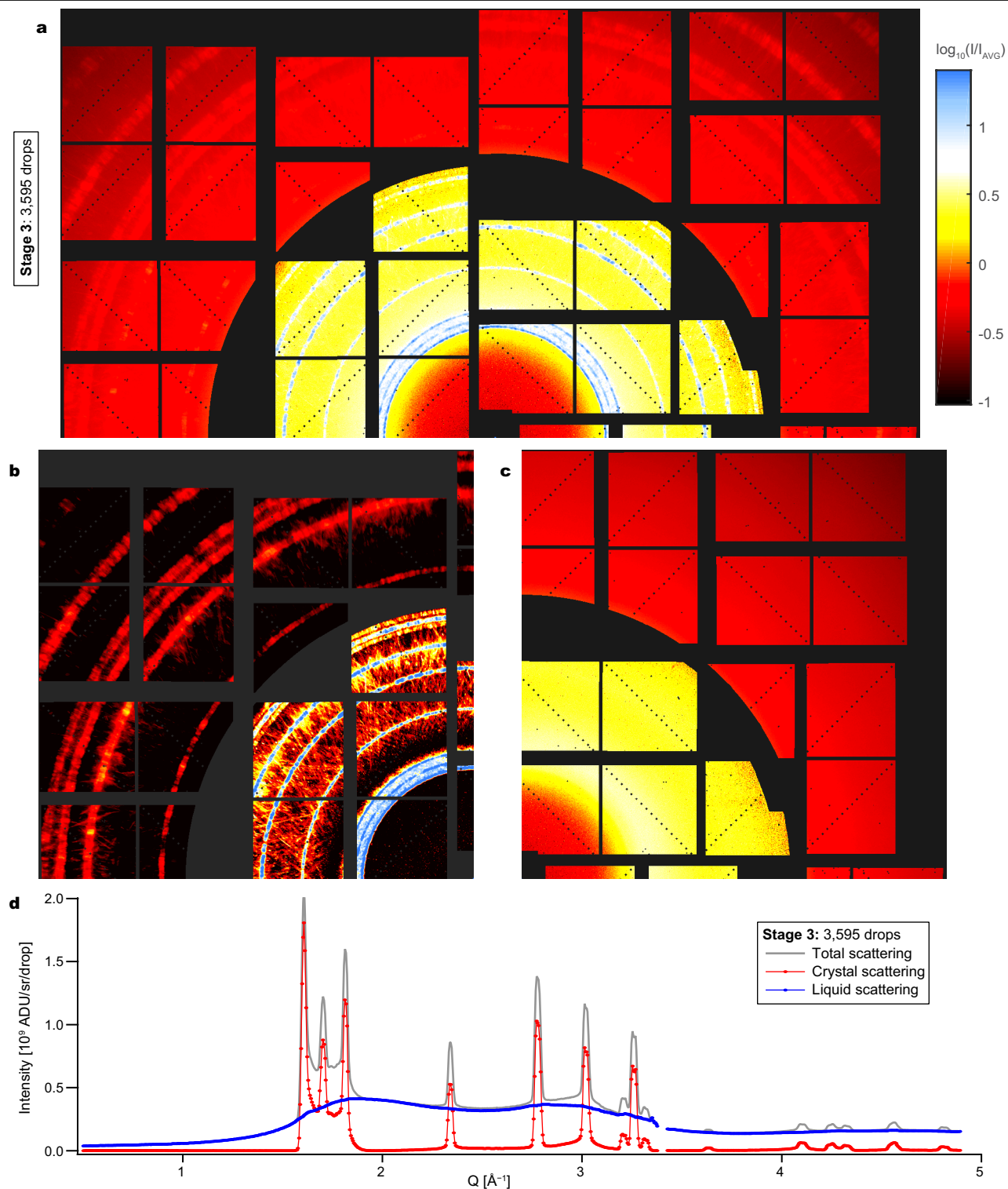
Extended Data Fig. 6 | Separation of X-ray scattering into crystal and liquid components. a, Accumulated X-ray detector image from stage 3 drops (top half of the detector). **b**, Corresponding separated image containing only the crystal diffraction. The intensity scale is shifted by −0.5 compared with **a. c**, Corresponding separated image containing only the liquid-scattering component. The intensity scale is the same as in **a. d**, Total and separated scattering profiles.
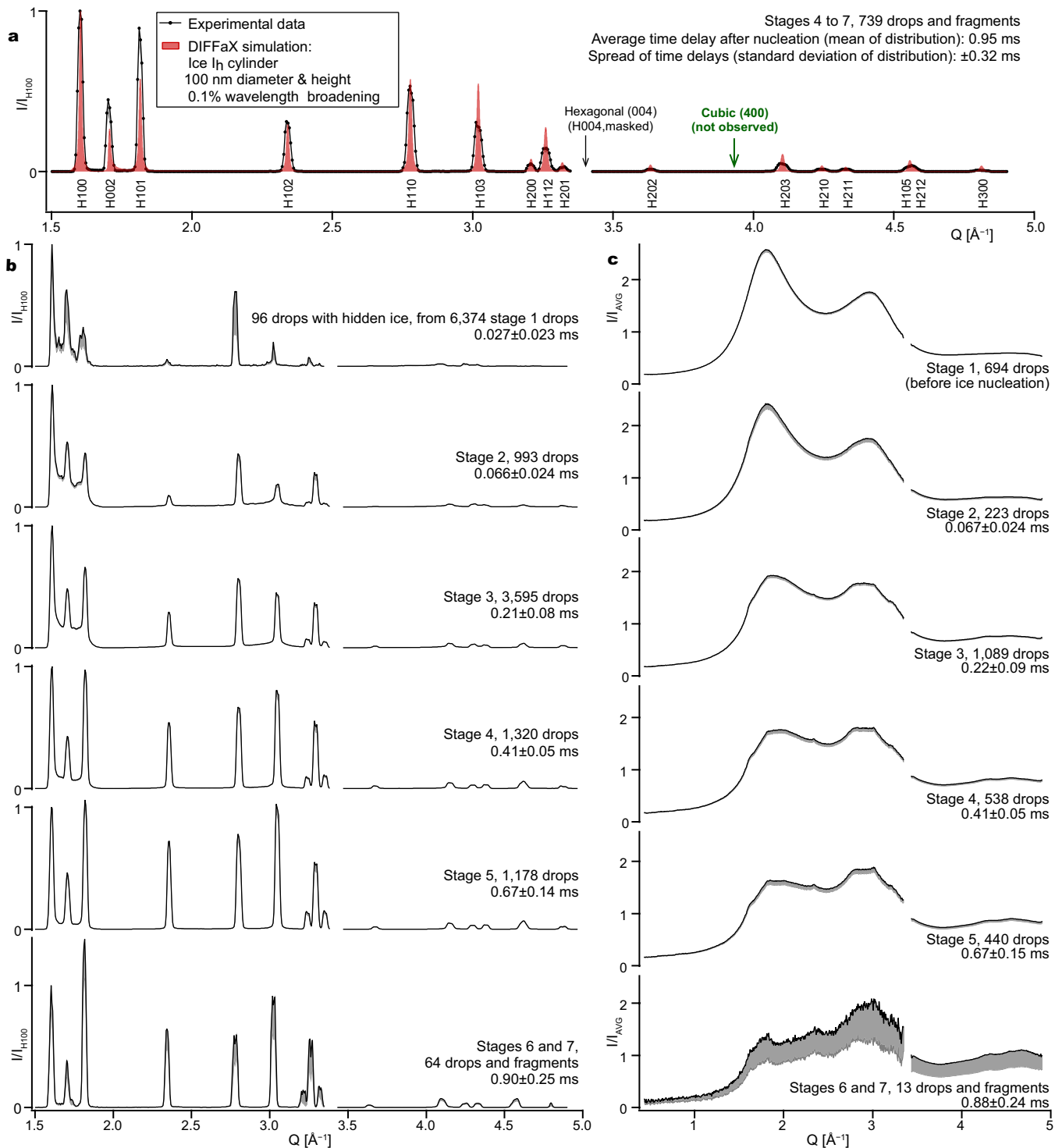
Extended Data Fig. 7 | X-ray crystal diffraction and liquid scattering during freezing. a, X-ray diffraction from drops in the last four stages of freezing, recorded with 0.01 mJ XFEL pulses. These data were not affected by detector saturation. The panel also shows simulated diffraction pattern from a nanocylinder of hexagonal ice; the relative heights of the first three peaks are different from those simulated for bulk hexagonal ice[9]. **b**, Evolution of X-ray diffraction from ice crystals, 0.13 mJ XFEL pulses. The height of some peaks was affected by saturation. **c**, Evolution of diffuse X-ray scattering from the liquid, 0.42 mJ XFEL pulses. The liquid-scattering data were not affected by saturation. In all panels, the standard deviations of experimental data, evaluated by means of bootstrapping over bands with $\Delta Q = 0.0025\,\text{Å}^{-1}$, are shown as lower confidence bands at one standard deviation (Methods).

Article
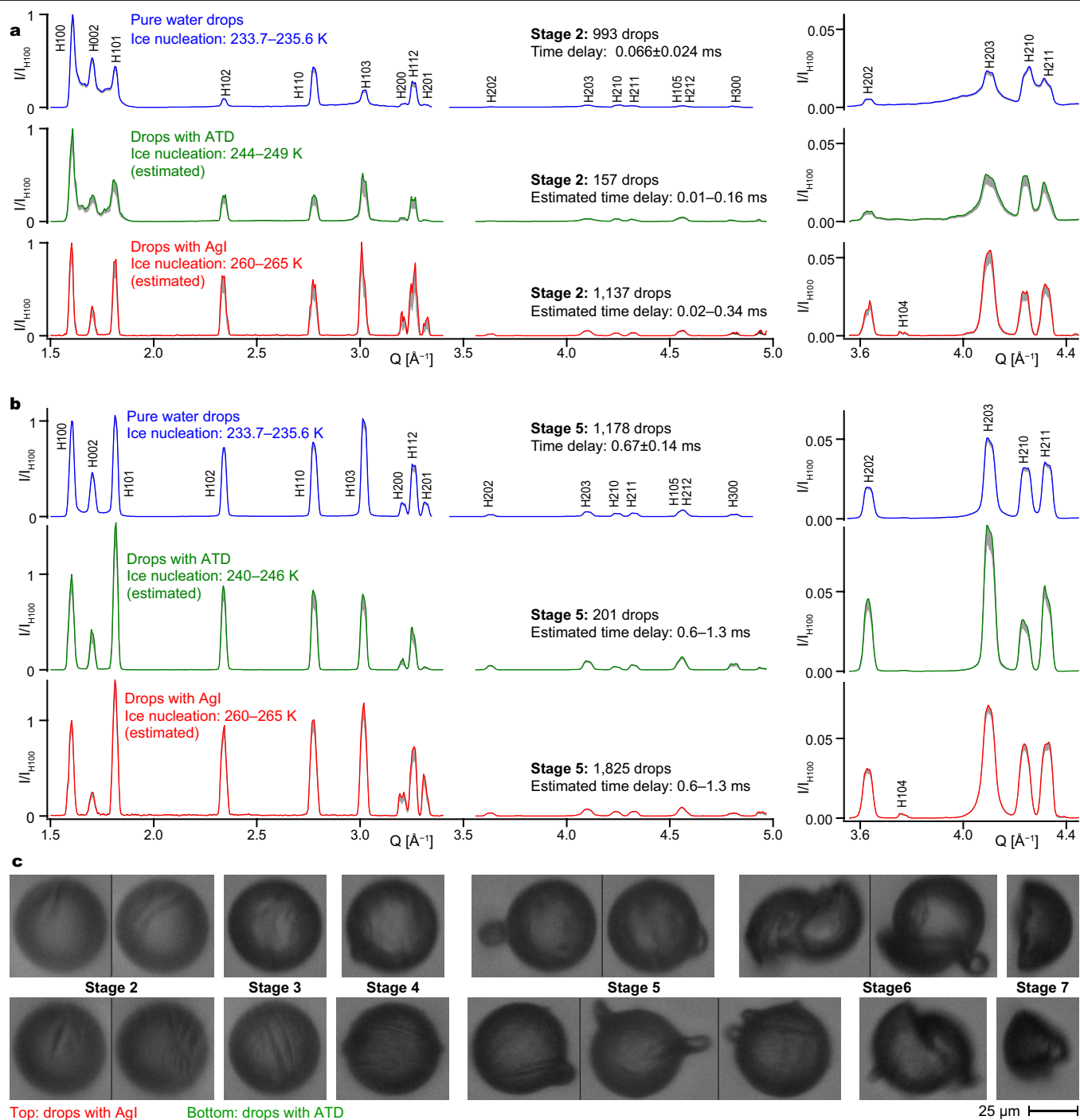
Extended Data Fig. 8 | Freezing after heterogeneous nucleation. a, Diffraction from stage 2 drops of pure water (0.13 mJ XFEL pulses), doped with ATD (0.14 mJ) and doped with AgI (0.12 mJ). **b**, Diffraction from stage 5 drops of pure water (0.13 mJ), doped with ATD (0.03 mJ) and doped with AgI (0.04 mJ). The left-side graphs in **a** and **b** show the entire Q range and the right-side graphs are zoom-ins on the lower-height peaks at large Q. In panels **a** and **b**, the standard deviations, evaluated by means of bootstrapping over bands with $\Delta Q = 0.0025\ \text{Å}^{-1}$, are shown as lower confidence bands at one standard deviation (Methods). **c**, Stages of freezing for drops doped with ATD and AgI. See the Supplementary Information for a description of how they differ from the freezing stages of pure water drops.
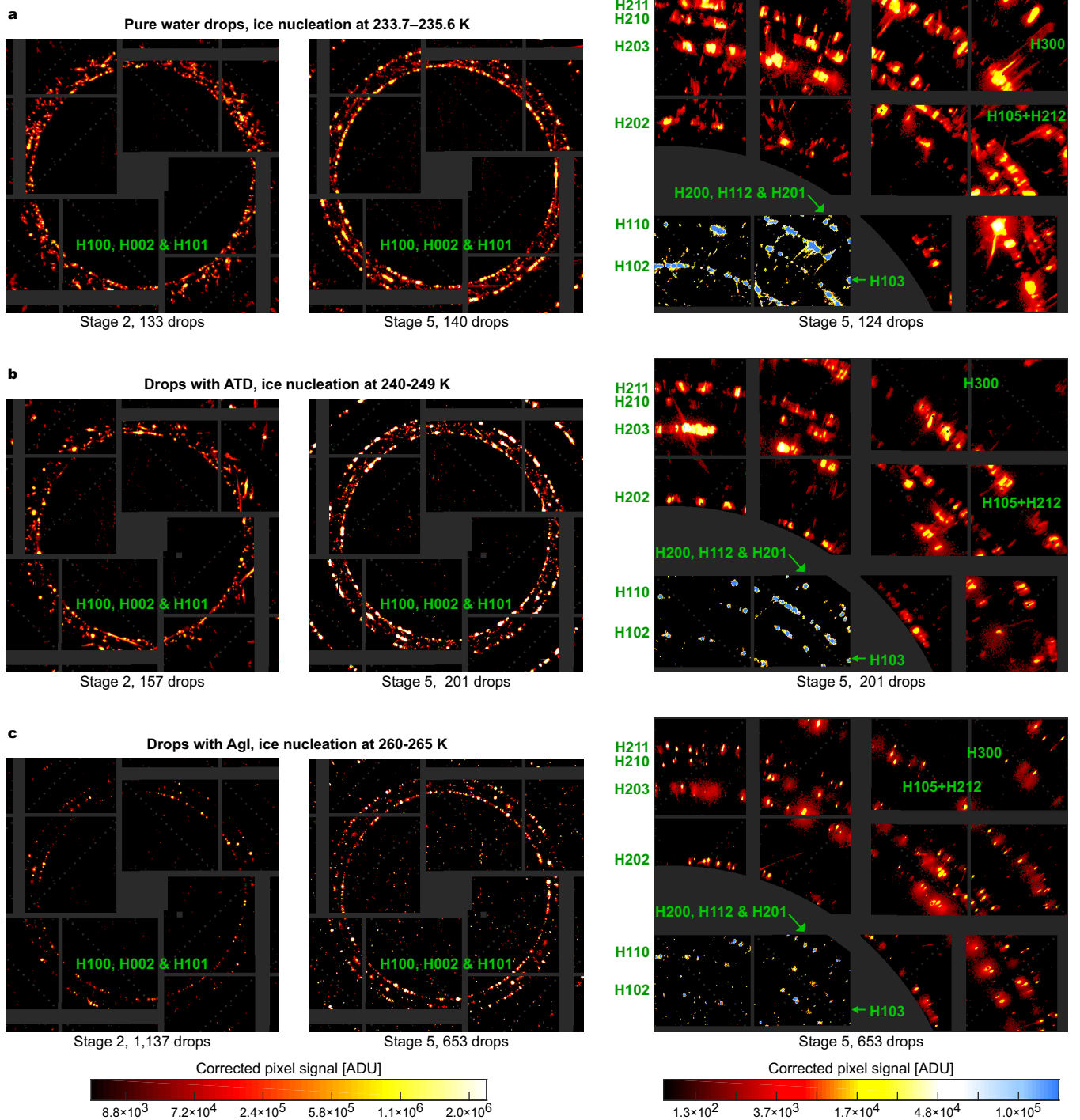
Extended Data Fig. 9 | Distribution and shapes of diffraction spots at different freezing temperatures and time delays. From left to right, the figure shows accumulated diffraction images of the first three diffraction rings during stages 2 and 5 and of the rings at medium and high diffraction angles during stage 5. **a**, Pure water drops. During stage 2, the rings are not well defined because of spots from strongly strained crystals that appear between the rings. The spots at large diffraction angles show a large radial elongation owing to inhomogeneous strain within single crystals. **b**, Drops with ATD. The spots are similar to those from pure water. **c**, Drops with AgI. There are substantially fewer diffraction spots per drop and the first three rings are already well defined during stage 2, indicating a higher degree of long-range order. The brightest spots at large angles are less elongated radially, indicating less inhomogeneous strain over the approximately 1-μm-diameter regions investigated by the XFEL beam.

Article

Extended Data Table 1 | Freezing-model parameters for 40-µm drops freezing in vacuum after homogeneous ice nucleation, determined by fitting experimental data with the droplet-freezing model

Parameter	Value	Statistical uncertainty	Description
		Freezing model parameters	
J_1	16.83	±0.03	Parametrized homogeneous ice nucleation rate J_N
J_2	−1.5	±0.1	$J_N\ [\mathrm{m^{-3}s^{-1}}] = 10^{J_1+J_2(T-234.55\ \mathrm{K})}$
V_{grow}	0.27 m/s	±0.03 m/s	Ice dendrite growth velocity
t_{34}	0.18 ms	±0.02 ms	Fixed duration of stage 3 (before spicules appear)
t_{45}	0.18 ms	±0.03 ms	Fixed duration of stage 4 (spicule growth up to a height threshold of 2.7 µm)
P_{56}	0.05	−0.04; +0.06	Probability of droplets cracking without separation
P_{57}	0.60	±0.04	Probability of droplets splitting into fragments
t_{56mean}	0.39 ms	±0.15 ms	Mean of normally-distributed elapsed time between threshold spicules and cracking
t_{56std}	0.17 ms	−0.17 ms; +0.31 ms	Standard deviation of normally-distributed elapsed time between threshold spicules and cracking
t_{57mean}	0.54 ms	±0.02 ms	Mean of normally-distributed elapsed time between threshold spicules and splitting
t_{57std}	0.30 ms	±0.04 ms	Standard deviation of normally-distributed elapsed time between threshold spicules and splitting
		Auxiliary experimental parameters characterizing the observability of freezing stages	
R_{vis}	13 µm	±2 µm	Actual radius of the visible region inside the drop
d_{Xmin}	2 µm	±2 µm	Minimum size of detectable ice or liquid regions
Y_{DOF}	12 µm	−5 µm; +4 µm	Effective depth of field for observing dendrites
P_{4H}	0.10	−0.10; +0.11	Probability of a stage 4 drop not displaying spicules
P_{5H}	0.015	−0.015; +0.09	Probability of a stage 5 drop not displaying spicules